LANGMUIR

pubs.acs.org/Langmuir Article

Understanding How Coacervates Drive Reversible Small Molecule Reactions to Promote Molecular Complexity

Michael I. Jacobs, Edward R. Jira, and Charles M. Schroeder*

Cite This: *Langmuir* 2021, 37, 14323−14335 Read Online

ACCESS | Metrics & More | Article Recommendations | Supporting Information

ABSTRACT: Liquid−liquid phase-separated coacervate droplets give rise to membraneless compartments that play an important role in the spatial organization and reactivity in cells. Due to their molecularly crowded nature and ability to sequester biomolecules, coacervate droplets create distinct environments for enzymatic reaction kinetics and reaction mechanisms that markedly differ from bulk solution. In this work, we use a combination of experiments and quantitative modeling to understand how coacervate droplets promote reversible small molecule reaction chemistry. In particular, we study a model condensation reaction generating an unstable fluorescent imine in polyacrylic acid−polyethylene glycol coacervate droplets over a range of conditions. At equilibrium, the concentration of the imine product in coacervate droplets is approximately 140-fold larger than that in bulk solution, which arises due to preferential partitioning of reactants and products into coacervate droplets and a reaction equilibrium constant that is roughly threefold larger in coacervate droplets than in solution. A reaction−diffusion model is developed to quantitatively describe how competing reaction and partitioning equilibria govern the spatial distribution of the imine product inside coacervate droplets. Overall, our results show that compartmentalization stabilizes kinetically labile reaction products, which enables larger reactant concentrations in coacervate droplets compared to bulk solution. Broadly, these results provide an improved understanding of how biomolecular condensates promote multistep reaction pathways involving unstable reaction intermediates and suggest how coacervates provide a potential abiotic mechanism to promote molecular complexity.

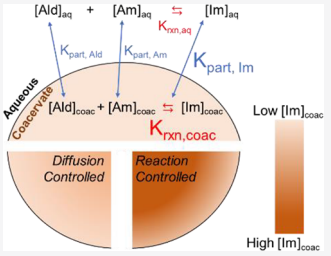

INTRODUCTION

Biomolecular condensates have recently been recognized to play an important role in the spatial organization and reactivity in cells.[1] Membraneless compartments have been associated with several biological functions including cell signaling[2,3] and transcription.[4,5] Within cells, these condensates are formed via liquid−liquid phase transitions due to the interactions between proteins (frequently with intrinsically disordered regions) and nucleic acids. Intracellular condensates can exist constitutively or arise at specific points during the cell cycle or in response to stimuli.[6] Due to their ability to provide compartmentalization without the use of a membrane bilayer, membraneless compartments have been proposed as a prebiotic means of molecular organization that could promote origin of life chemistry.[7,8] Although biomolecular condensates can operate as open reactors that promote transport across their boundaries, the mechanisms by which they can modulate chemical and biochemical reactions remain unclear.[9]

Coacervates are frequently used as model systems to explore how liquid−liquid phase separation influences biochemical processes within cells or promotes origin of life chemistry.[10] Coacervates are dense liquid droplets composed of macromolecules that separate from the dilute phase through liquid−liquid phase separation either by segregation or association.[11,12] Significant recent work has been directed toward understanding how coacervate droplets influence biomolecular enzymatic reactions.[9,13,14] Prior work has reported accelerated biochemical reaction rates in coacervates and coacervate-containing solutions. Some observations of enhanced reaction rates are attributed to partitioning of biomolecules within coacervates, resulting in large localized concentrations of enzymes and reactants.[15−20] However, the macromolecularly crowded and highly charged coacervate environment has also been reported to change reaction kinetics by potentially altering biomolecule conformations and reaction pathways.[17,21−24] For example, in polyethylene glycol (PEG)-based coacervates, T7 RNA polymerase was reported to have an association constant 2 orders of magnitude larger and a transcription rate constant 6 times larger than in buffered solution.[23] By taking advantage of the ability to co-localize multiple biomolecules, prior work has examined how coacervates accelerate multistep chemical reactions.[25−27] In addition to enzymatic biomolecular chemistry, a few prior studies have shown that coacervates also promote non-biological catalyzed reactions such as nanoparticle-catalyzed reactions,[15,28,29] though the majority of prior studies has

Received: August 20, 2021
Revised: November 16, 2021
Published: December 2, 2021

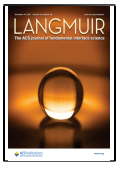

https://doi.org/10.1021/acs.langmuir.1c02231
Langmuir 2021, 37, 14323−14335

mainly focused on understanding how coacervation affects enzyme activity.

Prior work has shown that small molecules readily partition into coacervate droplets, resulting in localized increases in the concentration of small molecules in the coacervate phase.[15,30−35] Moreover, it has been hypothesized that changes in enzymatic activity within molecularly crowded environments arise from interactions of both the enzyme and small molecule substrates with the molecular crowder.[36] The chemical environment in coacervate droplets is expected to be significantly different compared to buffered solutions: in some cases, the water content is expected to be approximately 30−40% smaller than that found in bulk water[37] and the dielectric constant is closer to methanol than that of bulk water due to the high concentration of polymeric species.[19,38] Such differences in composition suggest that coacervate droplets could alter small molecule reaction kinetics or shift reaction equilibria through macromolecular-mediated interactions. Moreover, coacervate-driven changes in small molecule reaction kinetics or energetics are biologically relevant. For example, substrate channeling between multiple enzymes might be promoted if the unique hydration environment found in coacervates stabilizes labile intermediates in an enzymatic reaction pathway.[39] Despite recent progress, we lack a full understanding of how coacervation influences small molecule reaction chemistry.

To understand how reactions in coacervates change small molecule reaction kinetics and energetics, we study an imine synthesis reaction (Scheme 1) in coacervate droplets composed of polyacrylic acid (PAA) and PEG. Imine chemistry has previously been shown to control templated assembly of peptide condensation in self-induced biomolecular condensates as a means of generating chain-length-specific oligomers.[40] PAA-PEG systems were previously shown to form H-bond-driven coacervate droplets capable of sequestering various small molecules.[32,41] Here, we show how PAA-PEG coacervate droplets create regions of high imine synthesis reactivity at several different solution compositions through both partitioning of reactants and shifts in reaction equilibria. A reaction−diffusion model is developed and used to understand how reaction and partitioning equilibria control the concentration of reaction products in coacervate droplets. Broadly, our results suggest that the ability of coacervate droplets to accumulate unstable reaction products could further elucidate the role of biomolecular condensates in cells and provide an increased understanding of how coacervates could drive origin of life chemistry.

Scheme 1. Reversible Synthesis of Fluorescent Imine 3 from Non-Fluorescent Reactants Amine 1 and Aldehyde 2

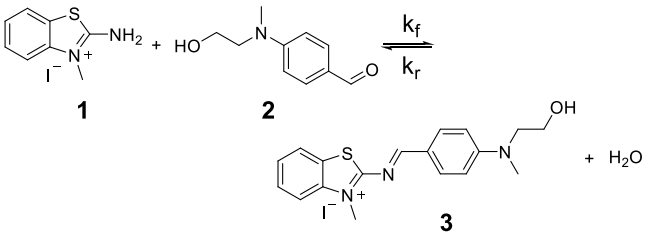

EXPERIMENTAL SECTION

Materials. Poly(ethylene glycol) (PEG, $M_w \approx 35$ kDa) was purchased from Sigma-Aldrich. Poly(acrylic acid) (PAA, $M_w \approx 240$ kDa) was purchased from Alfa-Aesar. *N*-Methyl-*N*-(2-hydroxyethyl)-4-aminobenzaldehyde **2** was purchased from AA Blocks LLC and used without further purification. *N*-Methyl-2-amino-benzothiazolium salt **1** was synthesized as previously described (details in the Supporting Information).[42,43] The kinetically stable dye analog (**4**) of imine **3** (which replaces the imine functional group with an alkene) was synthesized as previously described (structure and details in the Supporting Information).[44]

Bulk Imine Synthesis Kinetics Measurements. Bulk imine synthesis reaction kinetics were measured using both UV−vis and fluorescence spectroscopies in aqueous buffer solution (50 mM citrate, pH 3) and in the presence of individual coacervate components (PAA or PEG). All measurements were performed at ambient temperature (295 K). The quantum yield of dye **4** has previously been reported to be environmentally sensitive.[44] Similarly, the relative quantum yield of imine **3** was measured to change with different environmental conditions (Figure S1). To avoid solvatochromic effects that may give rise to errors in quantifying imine concentrations using fluorescence emission, UV−vis absorption spectroscopy was used to quantify imine **3** concentration in bulk solution to measure the aqueous imine synthesis reaction equilibrium constant $K_{rxn,aq}$. The absorption maximum of imine **3** was measured to be $\lambda_{abs,max} = 530$ nm in aqueous solution. Although the absorption peak was slightly shifted between species **3** and **4**, the incorporation of an imine bond into the conjugated polymethine chain reportedly has a limited effect on the molar absorption coefficient of the dye (i.e., molar absorptivities are on the same order of magnitude).[42] Therefore, the molar absorptivity of dye **4** in aqueous solution was determined to be $\varepsilon_{510} = (5.42 \pm 0.09) \times 10^4\ M^{-1}\ cm^{-1}$ (Figure S2), and this value of molar absorptivity was used to quantify the concentration of imine **3** at equilibrium. The same molar absorptivity and procedure were used to calculate the concentration of imine **3** at equilibrium in aqueous solution and in coacervate phases (as described below). Therefore, although this approximation may introduce some uncertainty in determining absolute reaction equilibria values, it has no effect on relative comparisons between different reaction equilibria values.

UV−vis measurements were performed with a 10 mm cuvette using a Nanodrop One spectrophotometer (ThermoFisher Scientific, Inc.). Amine **1** and aldehyde **2** were mixed in equimolar concentrations, and absorbance at 530 nm was measured every 4 s until equilibrium was reached (typically within 10−15 min), as denoted by a plateau in transient absorbance. Due to higher sensitivity, fluorescence spectroscopy was used to quantify reaction rates k_r. Fluorescence intensity was measured every 4 s with a fluorometer (Cary Varian) with excitation and emission wavelengths of 515 and 550 nm, respectively. The expected imine **3** concentrations at equilibrium (determined from experimentally measured $K_{rxn,aq}$ values) were used to relate fluorescence intensity and concentration of imine **3** for each solution condition. An integrated bimolecular rate law was used to determine the forward k_f and reverse k_r rate constants from the fluorescence data as described in the Supporting Information.

Coacervation Turbidity Assay. PAA and PEG were dissolved in 50 mM citrate buffer (pH 3) to a final concentration of 0.25 mg/mL. PAA and PEG solutions were mixed at PAA mass fractions (f_{PAA}) ranging from 0 to 1 in increments of 0.1. Solutions were mixed in 10 mm cuvettes and allowed to equilibrate for 15 min before measuring turbidity (absorption at $\lambda = 600$ nm) as a marker for phase separation using a Nanodrop spectrophotometer. Ultimately, $f_{PAA} = 0.6$ showed the highest turbidity (Figure S3) and was used throughout the experiments, unless otherwise noted.

Small Molecule Partitioning in PAA-PEG Coacervates. PAA and PEG were mixed ($[\text{macromolecule}]_{total} = 33$ mg/mL, $f_{PAA} = 0.6$,) in 1.5 mL conical centrifuge tubes in the presence of NaCl (0−1 M) and individual small molecules (amine **1** and aldehyde **2** at a concentration of 5 mM or dye **4** at a concentration of 60 μM). All

https://doi.org/10.1021/acs.langmuir.1c02231
Langmuir 2021, 37, 14323−14335

samples were prepared in buffer solution (50 mM citrate, pH 3) to a total volume of 200 μL. The coacervate mixture was mixed by agitation and allowed to incubate for at least 1 h to establish partitioning equilibrium. Samples were spun at 15,000 rpm (~18,000*g*) for 15 min, and the supernatant was quantitatively removed from the coacervate. The mass of the pelleted coacervate was measured by determining the difference in weight between the empty and coacervate-containing centrifuge tubes. The coacervate pellet was dissolved in dimethylformamide (DMF) by shaking and heating the solution to 60 °C. Absorption spectra of the supernatant and dissolved coacervate solutions were measured using a Nanodrop spectrophotometer. Characteristic absorbance peaks from amine **1**, aldehyde **2**, and dye **4** (287, 350, and 510 nm, respectively; Figure S4) were used to quantify the concentration of the small molecules in the supernatant and coacervate solutions. The concentration of the small molecules in the coacervate phase was determined from the measured concentration in the dissolved coacervate solution and the mass of the coacervate (assuming a density close to 1 g/mL). The partitioning coefficient K_{part} for each small molecule was calculated as:

$$K_{part} = \frac{[\text{small molecule}]_{coac}}{[\text{small molecule}]_{aq}} \quad (1)$$

where $[\text{small molecule}]_{coac}$ and $[\text{small molecule}]_{aq}$ are the measured concentrations of the small molecules in the coacervate and aqueous phases, respectively. Partitioning coefficient measurements for each small molecule at each NaCl concentration were measured in triplicate.

Imine Reaction Equilibrium in PAA-PEG Coacervates. The imine synthesis reaction equilibrium constant in the PAA-PEG coacervate phase $K_{rxn,coac}$ was determined by mixing amine **1** and aldehyde **2** with PAA-PEG coacervate ([macromolecule] = 30 mg/mL, f_{PAA} = 0.6) in an Eppendrof UVette. The concentration of PAA-PEG was chosen such that there would be roughly ~60 μL of coacervate in solution. After incubating and reacting for ~2 h, the cuvette was spun at 6000*g* for 20 min to collect the coacervate. Although initially visibly opaque, the coacervate clarified over the course of several days, and UV−vis measurement was collected across the short path length (2 mm) of the cuvette. It was assumed that the reactant concentrations are determined by their respective partitioning coefficients during the clarification process. The concentration of imine **3** was determined as described above, and $K_{rxn,coac}$ was determined using the concentrations of amine **1** and aldehyde **2** in the coacervate (details in the Supporting Information). To ensure that the concentration of imine **3** measured in the coacervate phase was representative of that at reaction equilibrium, the concentration of imine **3** in the coacervate was measured both with and without the aqueous supernatant. The samples equilibrated for 2−3 days after any change was made.

Coacervate Imaging and Fluorescence Recovery after Photobleaching (FRAP). Two types of samples were analyzed using a confocal microscope: coacervate droplets with reactants in aqueous buffer and non-immersed coacervate droplets with reactants without buffer. To prepare the samples, amine **1** and aldehyde **2** (15 mM each) were mixed with NaCl (0−1 M) and PAA/PEG coacervate ([macromolecule] = 2 mg/mL, f_{PAA} = 0.6) in 50 mM citrate buffer, pH 3. Mixtures were incubated for 15−20 min before preparing microscope slides. To prepare the coacervate sample without buffer, a 20 μL droplet of the coacervate solution was deposited onto a clean microscope coverslip. The drop sat for 2−3 min (to allow coacervate droplets to gravitationally settle on the microscope slide) before a piece of filter paper was used to wick the buffer, leaving a non-immersed coacervate residue. To prepare the coacervate sample in buffer, a second 4 μL droplet of the coacervate mixture was immediately deposited directly adjacent to the non-immersed coacervate sample. A piece of double-sided tape (~150 μm-thick, 3M) with a hole cut out in the center was placed around both the non-immersed and immersed coacervate droplets, and a microscope slide was placed on top to create a sealed chamber containing both drops. The procedure to deposit the second drop and seal the chamber was performed rapidly (<1 min) to minimize potential water evaporation from the non-immersed coacervate droplets. Because both the non-immersed and immersed coacervate samples were in the same sealed environment, the relative humidity in the chamber equilibrated to the water activity of the immersed sample, and there was no evaporation expected from the non-immersed sample. Samples were prepared at least 30 min before imaging to allow the imine synthesis reaction to reach equilibrium.

Confocal microscopy imaging of coacervate samples containing reactants amine **1** and aldehyde **2** was performed on a Leica SP8 UV/visible confocal inverted microscope. All images were acquired with a 63×/1.40 HC PL APO Oil CS2 objective using Leica Application Suite X software (both from Leica). For all experiments, the excitation was at 515 nm and the emission bandwidth of the photomultiplier tube was set to 525−600 nm. To enable a quantitative comparison between samples, images were collected with a constant zoom factor, laser intensity, and photomultiplier voltage. To determine the relative concentration of imine **3** under different concentrations of NaCl, confocal images of the immersed coacervate samples were measured (at least 5 images per sample) and the average fluorescence intensity of similarly sized coacervate droplets (typically 10−20 μm in diameter) were measured. Confocal microscopy images were analyzed using FIJI (Fiji is just ImageJ) to determine average fluorescence intensity at each [NaCl].

FRAP measurements were performed on the confocal instrument with the same laser power and photomultiplier tube voltages used in the imaging experiments. Experiments were performed using the FRAP package in the LAS software. Two types of FRAP experiments were performed on both the immersed and non-immersed samples: partial droplet (5−10 μm bleached diameter) and whole droplet (~10 μm diameter). Typical measurements involved pre-bleach imaging for 10 frames, bleaching the region of interest (ROI) for 5−15 frames with laser power set to 100%, and imaging fluorescence recovery until complete. Post-bleach imaging was performed every 0.4 and 4 s for fast-recovering (immersed, diffusional controlled) and slow-recovering (non-immersed, reaction controlled) samples, respectively. FRAP measurements were performed in triplicate for each solution condition using a new ROI for each measurement.

Because of the loss of fluorescence during multi-frame post-bleach measurements, the fluorescence was normalized to a nonbleached ROI to obtain $F_N(t)$ as has been described previously:[45]

$$F_N(t) = \frac{[S_t - B_t]}{[R_t - B_t]} \frac{[R_0 - B_0]}{[S_0 - B_0]} \quad (2)$$

where S_t is the average measured fluorescence recovery of the bleached ROI. R_t is the average fluorescence intensity of a reference ROI that was either a similarly sized whole droplet in the same frame (for the whole-droplet experiments) or an ROI in the nonbleached region within the same droplet (for partial-droplet experiments). S_0 and R_0 are the average pre-bleach intensities for the bleached and nonbleached ROI, respectively. B_0 and B_t are the average background fluorescence pre- and post-bleaching, respectively. Recovery curves were fit using Python according to the following equation:

$$F_N(t) = A(1 - e^{-kt}) + C \quad (3)$$

where A is the mobile fraction of the fluorescent probe, C is the y-intercept of the $F_N(t)$ fluorescence intensity recovery curve, and k is the rate of recovery. For diffusion-controlled recovery, an apparent diffusion coefficient (D_{app}) was obtained using the recovery half-time ($\tau_{1/2} = \ln(2)/k$) and the radius (r) of the specific bleached ROI according to[46]

$$D_{app} = \frac{0.88r^2}{4\tau_{1/2}} \quad (4)$$

where 0.88 is a constant used for calculating diffusion of circular beams. For reaction-controlled recovery, the recovery rate k was taken to represent the reverse reaction rate constant k_r and was used to characterize reaction kinetics in coacervates.[47]

https://doi.org/10.1021/acs.langmuir.1c02231
Langmuir 2021, 37, 14323−14335

RESULTS AND DISCUSSION

To elucidate how coacervate droplets can accelerate chemical processes, we fully characterized reaction kinetics in aqueous solution, reaction kinetics in the coacervate environment, and the transport of reactants and products across the coacervate phase.[48] Figure 1 shows the relevant coupled equilibria (both

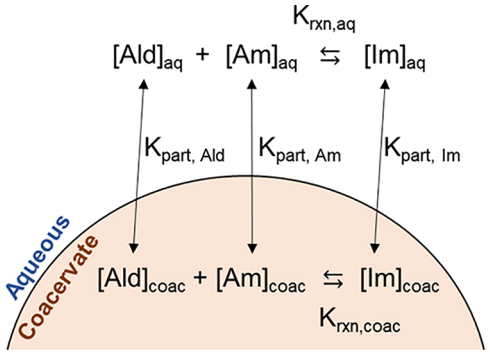

Figure 1. Coupled reaction and partitioning equilibria describing the reversible synthesis of fluorescent imine **3** in the PAA-PEG coacervate system. Imine synthesis can proceed in both aqueous solution and coacervate droplets as described by $K_{rxn,aq}$ and $K_{rxn,coac}$, respectively. Reactants and products partition into the coacervate phase, according to their partitioning equilibria constants, K_{part}.

reaction and partitioning) that describe the imine synthesis reaction in a liquid−liquid biphasic system. Reversible imine synthesis reaction energetics have previously been reported to shift in microcompartments due to reactions at an oil−water interface[49,50] and sequestration of reactants in micelles.[43] For these reasons, we used this model imine reaction to understand how compartmentalization drives condensation reactions to increase molecular complexity (i.e., higher energy or increased chemical diversity) in aqueous solution. The time scales of the competing equilibria shown in Figure 1 ultimately govern the distribution of reaction products in the coacervate system. Therefore, we experimentally measured each of the relevant equilibria in our reaction system. First, we describe the measurement of bulk reaction kinetics $K_{rxn,aq}$. We next measure reactant and product partitioning coefficients K_{part} followed by the measurement of reaction kinetics and energetics within coacervate droplets $K_{rxn,coac}$. Finally, using a coupled reaction−diffusion model, we fully characterize the concentration of reaction products within the coacervate droplets and use our model to explore how reversible reactions can be promoted via coacervation.

Imine Synthesis in Aqueous Solution. We began by studying the reaction between amine **1** and aldehyde **2** in bulk solution using UV−vis and fluorescence spectroscopies. Prior reports of imine synthesis of cyanine dye derivatives used fluorescence spectroscopy to measure reaction kinetics and quantify the product concentration under a variety of conditions.[43,49] However, the relative quantum yields of dye **4** and imine **3** change with viscosity[44] and solution composition (Figure S1), so UV−vis absorption spectroscopy was used to quantify the concentration of imine **3**. Fluorescence spectroscopy was only used to determine the unimolecular reverse rate constant k_r (Scheme 1) from calibrated fluorescence intensities.

The experimentally measured kinetic parameters of the imine synthesis reaction in aqueous solution (50 mM citrate buffer, pH 3) at different concentrations of NaCl are shown in Figure 2. Figure S5 shows kinetic traces of imine **3** synthesis at

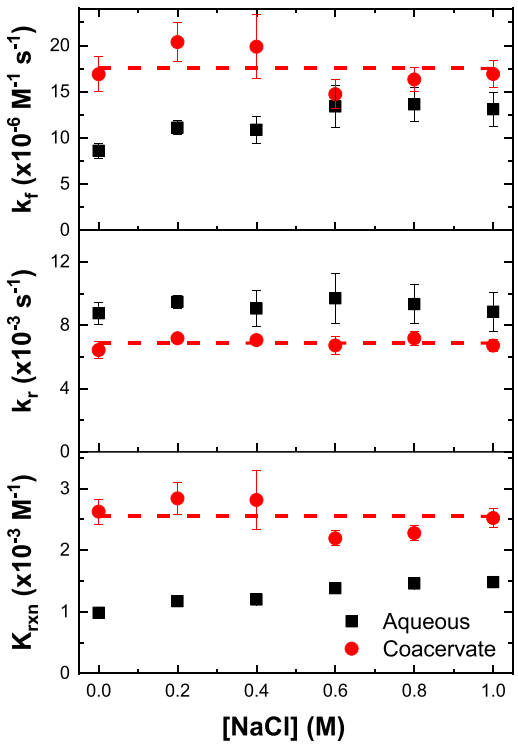

Figure 2. Experimentally determined reaction rate parameters K_{rxn}, k_r, and k_f in aqueous solution and in the bulk PAA-PEG coacervate phase. Dashed red lines represent the average of values across different NaCl concentrations used in the reaction−diffusion model and tabulated in Table S2.

different equimolar starting concentrations of amine **1** and aldehyde **2**. At 0 M NaCl, $K_{rxn,aq}$ in aqueous solution was determined to be $(9.8 \pm 0.5) \times 10^{-4}$ M^{-1}, which is approximately 2 orders of magnitude smaller than the reaction equilibrium constant measured for cyanine dye-derived imines.[43,49] We note that prior work only relied on fluorescence spectroscopy (rather than absorbance) to quantify the concentration of imine products, so apparent differences in $K_{rxn,aq}$ could arise from the method of quantifying reaction products (e.g., absorbance provides a quantitative method of determining concentrations), potential systematic errors introduced by using molar absorptivity of dye **4** to approximate that of imine **3**, or changes in reaction energetics. The forward k_f and reverse k_r rate constants for the synthesis of imine **3** at 0 M NaCl are $(8.6 \pm 0.8) \times 10^{-6}$ M^{-1} s^{-1} and $(8.8 \pm 0.7) \times 10^{-3}$ s^{-1}, respectively. Using these kinetic parameters, the concentration of imine **3** as a function of time was determined using an integrated reversible bimolecular rate law (Figure S5).

Imine synthesis reaction equilibria were previously reported to shift in the presence of oil−water interfaces[49,50] and anionic surfactants.[43] It is therefore necessary to determine $K_{rxn,aq}$ under a wide range of solution conditions (i.e., NaCl concentration and presence of coacervate components) used in this study. As shown in Figure 2 and Figure S6, $K_{rxn,aq}$ changes slightly upon increasing NaCl concentration. For example, $K_{rxn,aq}$ was determined to be $(1.48 \pm 0.05) \times 10^{-3}$ M^{-1} at 1.0 M NaCl, roughly 50% larger than the value at 0 M NaCl. Although k_r remains constant across all NaCl

https://doi.org/10.1021/acs.langmuir.1c02231
Langmuir 2021, 37, 14323−14335

concentrations examined in this work, k_f increases slightly with increasing salt concentrations, reaching a maximum value of $(1.3 \pm 0.2) \times 10^{-5}$ M^{-1} s^{-1} at 1.0 M NaCl. This slight change in $K_{rxn,aq}$ indicates that high concentrations of charged species might shift reaction equilibria within coacervate droplets.

In addition to characterizing the dependence of $K_{rxn,aq}$ on salt concentration, $K_{rxn,aq}$ was also measured in the presence of individual coacervate components (PAA and PEG). Although $K_{rxn,aq}$ does not change with increasing PEG concentration, it increases with increasing PAA concentration, reaching $(2.85 \pm 0.05) \times 10^{-3}$ M^{-1} at 20 mg/mL PAA (Figure S7). PAA has $pK_a = 4.5$[51] and exists primarily in its protonated state under these experimental conditions (pH 3). Together, these observations suggest that acidic species can shift imine synthesis reaction equilibria.[40] At low concentrations of PAA and PEG (<2 mg/mL; i.e., concentrations used to quantify reaction−diffusion in coacervates droplets, as described below), shifts in $K_{rxn,aq}$ are negligible and well approximated by the $K_{rxn,aq}$ values obtained in the absence of polymers.

Partitioning of Reactants and Products into PAA-PEG Coacervate Droplets. Small molecules such as fluorescent dyes have been observed to strongly partition into coacervate droplets.[31−35] The small molecule partition coefficient K_{part} can vary greatly depending on the chemical system. The propensity to partition is generally understood to arise from intermolecular interactions (e.g., hydrophobic, electrostatic, and H-bonding) between the small molecule and the macromolecules driving coacervation.[9] For some coacervate systems, the small molecule can affect the intermolecular interactions within the coacervate phase, leading to changes in K_{part} as a function of small molecule concentration.[33]

The partition coefficients of amine **1** ($K_{part,Am}$) and aldehyde **2** ($K_{part,Ald}$) were measured in PAA-PEG coacervate droplets. Unless otherwise noted, experiments were performed using a coacervate PAA mass fraction of $f_{PAA} = 0.6$. To determine whether K_{part} depends on the small molecule concentration for the PAA-PEG coacervate system, we prepared a series of solutions of PAA-PEG coacervates (15 and 25 mg/mL) containing different concentrations of amine **1** (0.5 and 1 mM) and aldehyde **2** (0.25 and 0.5 mM). After establishing partitioning equilibrium, the concentrations of small molecules in the coacervate and aqueous phases were determined and analyzed (Figure 3a). A linear relationship between the concentrations of amine **1** and aldehyde **2** in the coacervate and aqueous phases is observed, suggesting that K_{part} does not change with concentration for the small molecules used in this system. Thus, for all subsequent conditions, K_{part} was determined using a small molecule concentration similar to that used in the imine synthesis reactions.

We next studied the concentration dependence of the partition coefficients $K_{part,Am}$ and $K_{part,Ald}$ at different concentrations of NaCl (Figure 3b). Our results show that amine **1** and aldehyde **2** preferentially partition into the coacervate phase at all ionic strengths considered here (i.e., $K_{part} > 1$). In addition, $K_{part,Am}$ decreased with increasing concentration of NaCl, such that $K_{part,Am} = 9.2 \pm 0.2$ at 0 M NaCl and $K_{part,Am} = 5.5 \pm 0.2$ at 1.0 M NaCl. However, $K_{part,Ald}$ increased with increasing concentration of NaCl, such that $K_{part,Ald} = 5.3 \pm 0.3$ at 0 M NaCl and $K_{part,Ald} = 15.8 \pm 0.5$ at 1.0 M NaCl. A similar difference in partitioning behaviors in PAA-PEG coacervates as a function of NaCl concentration was previously reported for cationic and neutral dyes,[32] which suggests that different mechanisms drive the partitioning of the two reactants in this

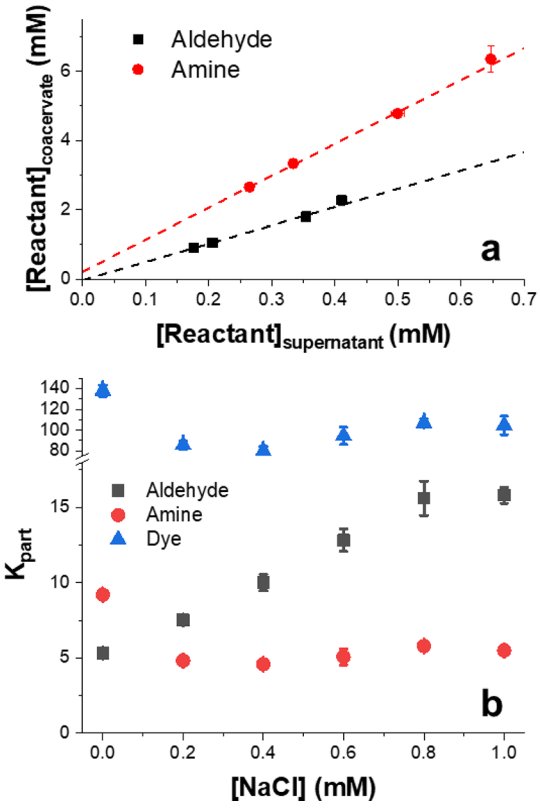

Figure 3. Concentration dependence and salt dependence of aldehyde and amine partitioning into the coacervate phase. (a) Concentrations of amine **1** and aldehyde **2** in the PAA-PEG coacervate phase versus the supernatant phase across a range of reactant concentrations. (b) Partitioning coefficients of amine **1**, aldehyde **2**, and dye **4** in PAA-PEG coacervates at different concentrations of NaCl.

system. Amine **1** is cationic, and its partitioning into PAA-PEG coacervates is primarily driven by H-bonding interactions. At higher salt concentrations, the pK_a and degree of protonation of PAA at pH 3 both decrease, causing a slight decrease in amine **1** partitioning.[32] Conversely, aldehyde **2** is nonionic, which suggests that its partitioning into PAA-PEG coacervates is driven primarily by hydrophobic interactions. At higher salt concentrations, the hydrophobicity of PAA-PEG coacervates has been observed to increase,[32] leading to a stronger hydrophobic driving force for nonionic partitioning. Overall, the concentrations of amine **1** and aldehyde **2** are both enhanced in PAA-PEG coacervates compared to bulk solution, and different NaCl concentrations change the total reactant concentration within the coacervate phase.

In addition to quantifying the partitioning of reactants, we further studied the partitioning of the imine reaction product between the coacervate and aqueous phases. Imine **3** forms in bulk solution and partitions into PAA-PEG coacervates, and it is therefore necessary to determine $K_{part,Im}$ to fully characterize the chemical reaction system. However, our results suggest that imine **3** is relatively unstable in aqueous solution, as its kinetic lifetime in aqueous solution is approximately 2 min as estimated from k_r. For these reasons, $K_{part,Im}$ cannot be directly measured in PAA-PEG coacervates. Instead, partitioning of dye **4** is used to approximate $K_{part,Im}$. Dye **4** differs from imine **3** by one C-atom, and estimates of their octanol−water partitioning coefficients K_{ow} are similar (Table S1),[52] suggesting that imine

https://doi.org/10.1021/acs.langmuir.1c02231
Langmuir 2021, 37, 14323−14335

3 and dye 4 have similar chemical characteristics and should partition similarly. The partitioning coefficient of dye 4 is large at 0 M NaCl (138 ± 5) and decreases with increasing concentration of NaCl (Figure 3b), suggesting that partitioning is driven primarily by H-bonding. The partitioning coefficient of dye 4 is significantly larger than those of amine 1 and aldehyde 2. Moreover, dye 4 retains the chemical functionality of both amine 1 and aldehyde 2. Together, these observations suggest that the Gibbs free energy of partitioning ΔG°_{part} of dye 4 can be approximated by the sum of ΔG°_{part} of its constituents (amine 1 and aldehyde 2). Therefore, the partitioning coefficient of dye 4 is expected to scale with the product of the partitioning coefficients of amine 1 and aldehyde 2, which is consistent with our experimental results.

Imine Synthesis Reaction Energetics and Kinetics in PAA-PEG Coacervates. After characterizing the concentrations of amine 1 and aldehyde 2 in the PAA-PEG coacervate system, we studied the imine synthesis reaction in the coacervate phase. First, the coacervate phase reaction equilibrium constant $K_{rxn,coac}$ was determined by measuring imine 3 at different reactant concentrations using UV−vis spectroscopy. Upon increasing the reactant concentration, the concentration of imine 3 in the PAA-PEG coacervate visibly increased (Figure 4a). Figure 4b shows the UV−vis spectra of the PAA-PEG coacervate phase at different reactant concentrations. The concentration of imine 3 in the coacervate phase was determined to be approximately 140 times larger compared to the aqueous phase. Product concentration enhancement in the coacervate likely arises (in part) due to an increased concentration of reactants in the coacervate phase compared to bulk solution. However, an increase in reaction product concentration in the coacervate phase can also arise from changes in reaction energetics due to the nature of the distinct chemical environment in coacervate droplets.

We further sought to determine if intermolecular interactions in the coacervate phase contribute to enhanced product concentrations. By plotting the concentration of imine 3 (determined from absorption at 530 nm) as a function of the product of reactant concentrations in the coacervate phase (calculated from the total reactant concentration in the cuvette, their partitioning coefficients, and the relative volume of the coacervate phase; Supporting Information), we determined the reaction equilibrium constant in the coacervate phase to be $K_{rxn,coac}$ = (2.6 ± 0.2) × 10^{-3} M^{-1} at 0 M NaCl (Figure 4c). It is possible that partitioning of imine 3 from the aqueous phase could interfere with quantification of $K_{rxn,coac}$, so the UV−vis absorption spectra were obtained with and without the aqueous supernatant present in the cuvette. Results from the UV−vis absorption spectra show that the concentration of imine 3 is nearly identical between the two conditions (Figure S8), suggesting that the imine 3 concentration measured under both conditions is largely determined by reaction equilibrium in the bulk coacervate phase. Moreover, $K_{rxn,coac}$ is approximately 2.7 times larger than $K_{rxn,aq}$, suggesting that imine synthesis in the PAA-PEG coacervate is slightly enhanced compared to bulk solution. $K_{rxn,aq}$ was also observed to increase with increasing PAA concentration (Figure S7). Therefore, we posit that the enhanced concentration of PAA in the coacervate phase promotes acid-catalyzed formation of imine 3.[40] Our results suggest that reactions in coacervates can generate enhanced concentrations of unstable chemical products that are not accessible in bulk solution due to a combination of increased concentration of reactants and intermolecular interactions with the polymeric species.

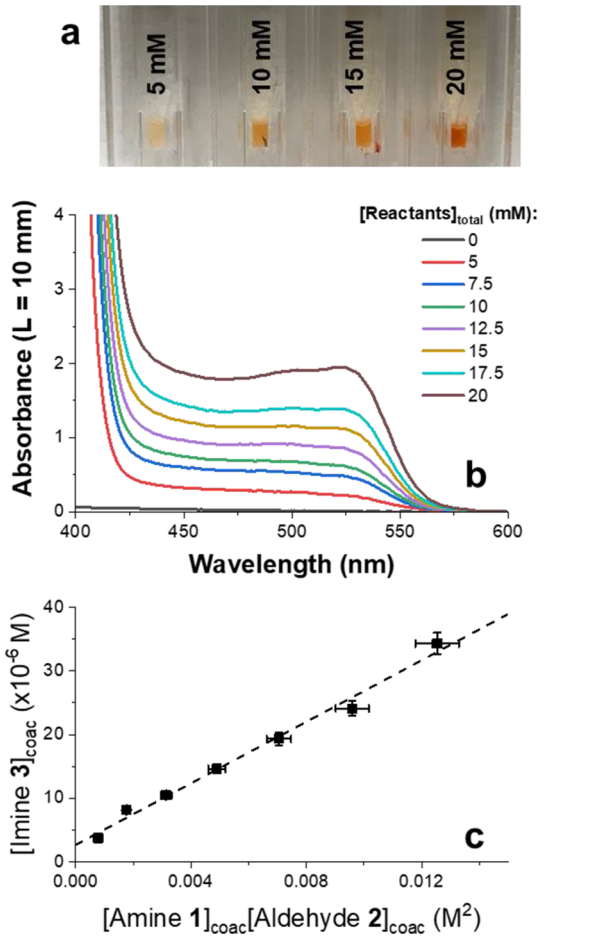

Figure 4. Imine synthesis reaction energetics and kinetics in PAA-PEG coacervates. (a) Series of images showing bulk PAA-PEG coacervate at different equimolar total reactant concentrations. (b) UV−vis absorption spectra of PAA-PEG coacervates at different equimolar total reactant concentrations. (c) Equilibrium imine 3 concentration in bulk PAA-PEG coacervates versus the product of reactant concentrations. The slope was used to calculate $K_{rxn,coac}$ in Figure 2.

We next assessed the ability of PAA-PEG coacervates to promote the synthesis of imine 3 under a variety of different solution conditions. Reaction equilibrium constants were measured in bulk PAA-PEG coacervates at different NaCl concentrations using the same methods and controls described above (Figures S8 and S9). As shown in Figure 2, $K_{rxn,eq}$ is enhanced in PAA-PEG coacervates at all concentrations of NaCl. Interestingly, even though both partitioning of the individual reactants and $K_{rxn,aq}$ vary considerably with changing NaCl concentrations, reaction energetics within the coacervate phase remain constant with changing solution conditions (e.g., average $K_{rxn,coac}$ = (2.5 ± 0.3) × 10^{-3} M^{-1}, dashed red line in Figure 2). These results suggest that the reaction environment within the coacervate phase remains relatively constant with changing ionic strength. These results are consistent with prior work reporting that the concentration of partitioned species in coacervates remains constant during wet-dry cycles,[53] and that coacervates can promote biochemical reactions under bulk conditions in which they are otherwise prohibited.[17] Overall, these results show that PEG-PAA coacervation provides a

https://doi.org/10.1021/acs.langmuir.1c02231
Langmuir 2021, 37, 14323−14335

means to maintain a constant, favorable reaction environment for the imine synthesis reaction across a range of solution conditions.

To further understand the increase in $K_{rxn,coac}$ compared to $K_{rxn,aq}$, we determined reaction rate constants for imine synthesis. To decouple imine **3** synthesis from partitioning to/from bulk solution, reaction kinetics were probed in individual coacervate droplets deposited on a glass coverslip without buffer solution. For these experiments, isolated coacervate droplets were sealed in a chamber with a drop of buffer solution, thereby minimizing water evaporation over the time scale of the characterization experiments. Imine synthesis reaction kinetics were determined by performing fluorescence recovery after photobleaching (FRAP) experiments on the individual coacervate droplets. Upon photobleaching entire isolated (non-immersed) coacervate droplets, fluorescence recovery only arises from chemical synthesis of new imine **3** (i.e., reaction dominant fluorescence recovery) because there is no suspending medium to replenish the photobleached imine **3**.[47,54] Thus, photobleaching whole, isolated droplets provides a method to trigger and measure imine synthesis reaction kinetics within coacervate droplets.

Figure 5a shows snapshots of an isolated photobleached coacervate droplet before, during, and after fluorescence recovery for 5 min. The rate of fluorescence recovery in isolated coacervate droplets was used to determine the reverse rate constant k_r in the coacervate environment (Figure 5c). The reverse rate constant k_r in PAA-PEG coacervates in 0 M NaCl solutions was found to be $(6.4 \pm 0.5) \times 10^{-3}$ s^{-1}, which is approximately 30% smaller than k_r measured in aqueous solution. Slower hydrolysis kinetics suggest that imine **3** is slightly stabilized relative to the hydrolysis transition state in PAA-PEG coacervate droplets, which arises from the decreased water concentration expected in the coacervate[37] and stabilizing interactions between imine **3** and acidic PAA.[40] We further determined k_f in PAA-PEG coacervates in 0 M NaCl solutions using values of $K_{rxn,coac}$ and k_r, and our results show that $k_f = (1.2 \pm 0.1) \times 10^{-6}$ M^{-1} s^{-1}, which is approximately 2 times larger compared to aqueous solution. Overall, our results show that k_r is slightly slower in the coacervate phase (suggesting stabilization of imine **3**) and k_f is slightly larger in the coacervate phase (suggesting stabilization of the transition state). Similar to $K_{rxn,coac}$, these individual rate constants do not change in the coacervate phase with changing NaCl concentration (Figure 2). Taken together, these observations suggest that the reaction environment in the coacervate phase remains similar with different solution properties.

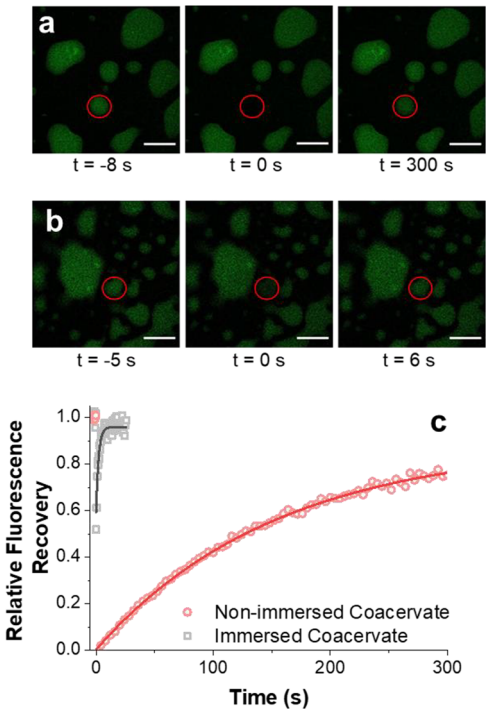

Figure 5. Whole droplet FRAP measurements. Images of fluorescence recovery of (a) a non-immersed and (b) immersed PAA-PEG coacervate droplets (from 2 mg/mL macromolecule, $f_{PAA} = 0.6$) at 0 M NaCl. Scale bars represent 20 μm. (c) Fluorescence recovery traces of non-immersed and immersed coacervate droplets. The slow fluorescence recovery in non-immersed coacervate droplets arises from imine synthesis and the fast fluorescence recovery in immersed coacervate droplets arises primarily from imine partitioning.

Small Molecule Reaction–Diffusion in PAA-PEG Coacervate Droplets. Although rate constants and energetics of imine synthesis have been systematically determined in the coacervate phase, these parameters alone cannot be used to describe reactions in coacervate droplets suspended in aqueous solution. FRAP measurements of suspended or immersed coacervate droplets (i.e., those surrounded by an aqueous medium) show qualitatively different recovery kinetics compared to non-immersed coacervate droplets (Figure 5b). Coacervate droplets immersed in aqueous solution show much faster recovery kinetics compared to similarly sized non-immersed droplets because the immersed coacervate droplet is in dynamic equilibrium with the surrounding solution, allowing mass transport across the interface.[45] Although non-immersed, isolated coacervate drops required chemical synthesis to recover fluorescence intensity, fluorescence intensity in immersed coacervates rapidly recovers as nonbleached imine **3** from bulk solution rapidly diffuses across the liquid–liquid interface and into the coacervate droplet. These qualitative observations suggest that fluorescence recovery in immersed coacervate droplets is primarily controlled by rates of diffusional mass transport instead of reaction equilibrium. We quantify the relative rates of reaction and diffusion using a dimensionless group known as the Damköhler number, as discussed below.

The relative concentrations of imine **3** in individual, immersed coacervate droplets were determined using confocal fluorescence microscopy. Figure 6a,b shows representative confocal microscopy images of immersed PAA-PEG coacervates droplets at 0 and 1.0 M NaCl, respectively. The fluorescence intensity is noticeably higher in coacervate droplets in 1.0 M NaCl compared to those in 0 M NaCl solution. The average fluorescence intensity in coacervate droplets at different NaCl concentrations is shown in Figure 6c. The average fluorescence intensity initially decreases with increasing NaCl concentration until 0.4 M NaCl, after which the fluorescence intensity increases upon increasing NaCl concentration. As described above, our results suggest that the chemical environment within PAA-PEG coacervate droplets remains relatively constant at different NaCl concentrations. Therefore, the average fluorescence intensity within droplets is expected to be proportional to the concentration of imine **3** under different solution conditions. Thus, relative fluorescence intensities of imine **3** are used to determine the relative

https://doi.org/10.1021/acs.langmuir.1c02231
Langmuir 2021, 37, 14323–14335

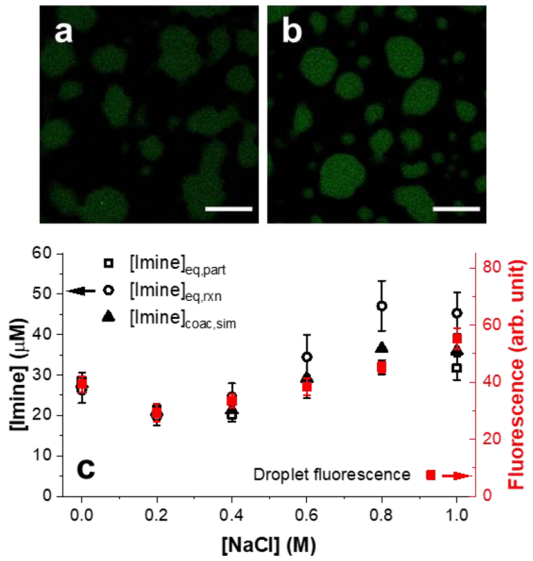

Figure 6. Confocal microscopy images of PAA-PEG coacervate droplets at (a) 0 M and (b) 1.0 M in solutions with 15 mM equimolar reactant concentrations and 2 mg/mL total macromolecule concentration. Scale bars represent 20 μm. (c) Average fluorescence intensity of 10−20 μm PAA-PEG coacervate droplets is plotted on the right-hand axis. Comparisons of equilibrium imine **3** concentrations arising from different equilibria processes in a 10 μm radius coacervate droplet at a volume fraction of 0.005 are shown on the left axis. $[\text{Imine}]_{\text{eq,part}}$ is the partitioning equilibrium concentration, $[\text{imine}]_{\text{eq,rxn}}$ is the reaction equilibrium concentration, and $[\text{imine}]_{\text{coac,sim}}$ is the average imine concentration from the reaction−diffusion model.

concentrations of imine **3** in PAA-PEG coacervates at different concentrations of NaCl. However, both reaction and molecular transport in coacervate droplets need to be quantified to understand absolute imine **3** concentrations in immersed coacervate droplets in aqueous solutions.

We next sought to quantify the relative influence of chemical reaction rates and molecular transport. The concentration of imine **3** in the coacervate phase is controlled by competing equilibria: reaction equilibria and partitioning equilibria of both reactants and products (Figure 1). The Damköhler number *Da* is a dimensionless group that compares relative time scales of reaction and transport in a chemical process. For the imine synthesis reaction, the Damköhler number is given by

$$Da = \frac{k_r r_{coac}^2}{\pi^2 D_{im}} \tag{5}$$

where D_{im} is the diffusion coefficient of the imine in the coacervate, assuming a spherical droplet of radius r_{coac}. When $Da \gg 1$, the rate of transport is much slower than the rate of reaction, and the concentration within the droplet can be approximated by reaction equilibrium (i.e., $[\text{imine}]_{\text{eq,rxn}}$). When $Da \ll 1$, diffusional mass transport is much faster than the reaction, and the concentration within the droplet can be approximated by partitioning equilibrium (i.e., $[\text{imine}]_{\text{eq,part}}$). When $Da \approx 1$, the rates of transport and reaction are approximately equal.

To quantify the regimes of reaction−transport for coacervate droplets, D_{im} was measured in PAA-PEG coacervate droplets at different NaCl concentrations by FRAP and photobleaching only portions of entire droplets. D_{im} was found to decrease with increasing NaCl concentration, ranging from $D_{im} = (1.5 \pm 0.2) \times 10^{-12}$ to $(9.4 \pm 0.2) \times 10^{-13}$ m^2 s^{-1} at 0 and 1.0 M NaCl, respectively (Figure S10). For a coacervate droplet with radius r_{coac} = 10 μm (characteristic droplet size in our experiments, as shown in Figure 6a,b), *Da* was found to be *Da* = 0.05 and 0.07 in 0 and 1.0 M NaCl, respectively. Thus, imine diffusion is faster than imine synthesis under all conditions. However, *Da* is not ≪ 1, so partitioning equilibrium is not expected to completely dominate the system. In other words, the imine synthesis reaction is expected to play a minor role in determining concentration profiles in the coacervate. Broadly, both reaction and diffusion need to be taken into account to accurately quantify imine synthesis in coacervates.

We next sought to quantify the concentration of imine **3** in coacervate droplets. The concentrations of imine **3** at reaction ($[\text{imine}]_{\text{eq,rxn}}$) and partitioning ($[\text{imine}]_{\text{eq,part}}$) equilibria were first compared to approximate concentrations in droplets with very large and very small *Da*, respectively. For this comparison, coacervate droplets were assumed to have a radius r_{coac} = 10 μm and exist at a volume fraction f_{coac} = 0.005, which is consistent with experimental conditions where $[\text{macromolecule}]_{\text{total}}$ = 2 mg/mL. Because $K_{rxn,aq}$ and $K_{rxn,coac}$ are generally small, the concentrations of amine **1** and aldehyde **2** were fixed at concentrations determined by their partitioning coefficients. First, $[\text{imine}]_{\text{eq,rxn}}$ was determined at each NaCl concentration using the concentrations of reactants in the coacervate droplet and the average value of $K_{rxn,coac}$ (Figure 6c). The concentration of $[\text{imine}]_{\text{eq,rxn}}$ increases with increasing concentration of NaCl, from 20 ± 2 to 35 ± 3 μM at 0 and 1.0 M NaCl, respectively. Next, $[\text{imine}]_{\text{eq,part}}$ was determined using the aqueous imine **3** concentration calculated from aqueous reactant concentrations and $K_{rxn,aq}$ and experimentally determined $K_{part,Im}$ (Figure 6c). These results show that $[\text{imine}]_{\text{eq,part}}$ is relatively constant with NaCl concentration, increasing from 22 ± 1 to 24 ± 2 μM at 0 and 1.0 M NaCl, respectively. At low concentrations of NaCl (≤0.4 M), $[\text{imine}]_{\text{eq,rxn}}$ and $[\text{imine}]_{\text{eq,part}}$ are approximately equal, which suggests that the concentration of imine **3** can be predicted by either partitioning or reaction equilibrium at all *Da*. However, $[\text{imine}]_{\text{eq,part}}$ is less than $[\text{imine}]_{\text{eq,rxn}}$ at high ionic strengths for concentrations >0.4 M NaCl, which suggests that the equilibrium concentration of imine **3** in coacervate droplets varies depending on *Da*. The average fluorescence intensity of imine **3** in 10 μm radius PAA-PEG coacervate droplets was nearly 40% smaller in 0 M NaCl solution compared to 1.0 M NaCl. This relative change is smaller than that predicted by $[\text{imine}]_{\text{eq,rxn}}$ (roughly 75%) but larger than that predicted by $[\text{imine}]_{\text{eq,part}}$ (roughly 10%). Although these two equilibria provide baselines for comparison, these results suggest that a detailed reaction−diffusion model is needed to accurately describe imine **3** concentrations within coacervates.

Quantitative Model for Reaction−Diffusion in Coacervate Droplets. To quantitatively describe the imine synthesis reaction in the coacervate and aqueous phases, a reaction−diffusion model was developed, which considers the partitioning of small molecules and reaction rates in each phase (Supporting Information). Reaction−diffusion models have been previously used to understand coupled and sequential enzymatic reactions in coacervate droplets.[25,26] Here, coacervate droplets are modeled as spheres suspended in a well-mixed aqueous phase. Assuming droplets are distributed uniformly in solution and do not coalesce, the volume of the aqueous phase is determined from the coacervate droplet

https://doi.org/10.1021/acs.langmuir.1c02231
Langmuir 2021, 37, 14323−14335

radius r_{coac} and volume fraction f_{coac}. Imine synthesis proceeds in both the aqueous and coacervate phases according to the following rate law:

$$r_{[\text{imine}],x} = k_{f,x}\left([\text{aldehyde}]_x[\text{amine}]_x - \frac{[\text{imine}]}{K_{rxn,x}}\right) \quad (6)$$

where $r_{[\text{imine}],x}$ is the rate of imine **3** formation, $k_{f,x}$ is the forward rate constant, $K_{rxn,x}$ is the reaction equilibrium constant, and the subscript x represents the phase (e.g., aqueous (aq) or coacervate (coac)). The concentrations of amine **1** and aldehyde **2** in the coacervate and aqueous phases are determined using their experimentally measured partition coefficients and f_{coac}. As noted above, the concentration of reactants is assumed to be constant because $K_{rxn,aq} \ll 1$ and $K_{rxn,coac} \ll 1$. In this way, changes in the concentration of imine **3** are quantitatively modeled.

The species conservation equation for imine **3** inside the coacervate droplet is given by a coupled reaction−diffusion equation:

$$\frac{\partial[\text{imine}]_{\text{coac}}}{\partial t} = D_{im}\nabla^2[\text{imine}]_{\text{coac}} + r_{[\text{imine}],\text{coac}} \quad (7)$$

which can be written in spherical coordinates as

$$\frac{\partial[\text{imine}]_{\text{coac}}}{\partial t} = D_{im}\left(\frac{1}{r^2}\frac{\partial}{\partial r}\left(r^2\frac{\partial[\text{imine}]_{\text{coac}}}{\partial r}\right)\right) + r_{[\text{imine}],\text{coac}} \quad (8)$$

To solve this partial differential equation, two boundary conditions and one initial condition are needed. In brief, the initial imine **3** concentration is zero, and the concentration of imine **3** is assumed to rapidly reach an equilibrium value at the coacervate/aqueous interface given by $K_{part,im}$, such that $[\text{imine}]_{\text{coac}}(r = r_{coac}, t) = K_{part,im}[\text{imine}]_{\text{aq}}(t)$. In this way, the solubility of imine **3** at the coacervate/aqueous phase boundary is set by a fixed ratio that is combined with a continuity of mass flux condition to ultimately determine the transport of imine **3** across the interface. The second boundary condition assumes symmetry about the origin. Because diffusion within the coacervate phase is much slower than that in the aqueous phase, the aqueous phase is assumed to be well mixed at all time points. The reaction−diffusion model was numerically solved using a custom Python code.

The reaction−diffusion model was used to determine the equilibrium concentration of imine **3** in PAA-PEG coacervates at different NaCl concentrations (Supporting Information). The experimentally determined parameters used in the model are given in Table S2. The simulated average equilibrium concentrations of imine **3** in the coacervate droplet at different NaCl concentrations are shown in Figure 6c. As expected, at low concentrations of NaCl (≤0.4 M), $[\text{imine}]_{\text{coac,sim}}$ agrees with those predicted by both reaction and partitioning equilibria. At larger NaCl concentration (>0.6 M), $[\text{imine}]_{\text{coac,sim}}$ falls between $[\text{imine}]_{\text{eq,rxn}}$ and $[\text{imine}]_{\text{eq,part}}$, suggesting that both reaction and transport contribute to the coacervate concentration. Figure 6c also shows that $[\text{imine}]_{\text{coac,sim}}$ more closely matches the relative changes in average fluorescence intensity in coacervate droplets than either $[\text{imine}]_{\text{eq,rxn}}$ and $[\text{imine}]_{\text{eq,part}}$. $[\text{Imine}]_{\text{coac,sim}}$ increases by 30% from 0 to 1.0 M NaCl, which more closely matches the 40% increase in fluorescence intensity. Slight differences in $[\text{imine}]_{\text{coac,sim}}$ and fluorescence intensity trends might arise from the approximated partition coefficients of imine **3** and small differences in the partitioning behavior of dye **4** and imine **3**. Ultimately, these results suggest that a complete characterization of both reaction kinetics and transport in both the coacervate and bulk solution phases is necessary to fully understand small molecule reaction kinetics and distribution within coacervate droplets.

Having validated our reaction−diffusion model, we sought to use our model to understand how coacervates can promote reversible chemistry under a variety of different conditions. First, to understand how reversible reactions in coacervates influence aqueous solution reactivity, the reaction−diffusion model was used to explore the system at different values of f_{coac} ranging from $f_{coac} = 5 \times 10^{-4}$ to 0.2 in a 10 μm radius coacervate drop (Figure 7). Two different scenarios were simulated: (1) $[\text{imine}]_{\text{eq,rxn}} \approx [\text{imine}]_{\text{eq,part}}$ (i.e., PAA-PEG coacervates at 0 M NaCl) and (2) $[\text{imine}]_{\text{eq,rxn}} \neq [\text{imine}]_{\text{eq,part}}$ (i.e., PAA-PEG coacervates at 1.0 M NaCl). For both scenarios, larger values of f_{coac} resulted in smaller concentrations of reactants in aqueous solution, which was associated with a concomitant decrease in the simulated aqueous imine **3** concentration ($[\text{imine}]_{\text{aq,sim}}$; Figure 7a). These results suggest that reactions in coacervates are unable to significantly increase aqueous concentrations of imine **3** because of its preferential partitioning into the coacervate phase and instability in aqueous solution.

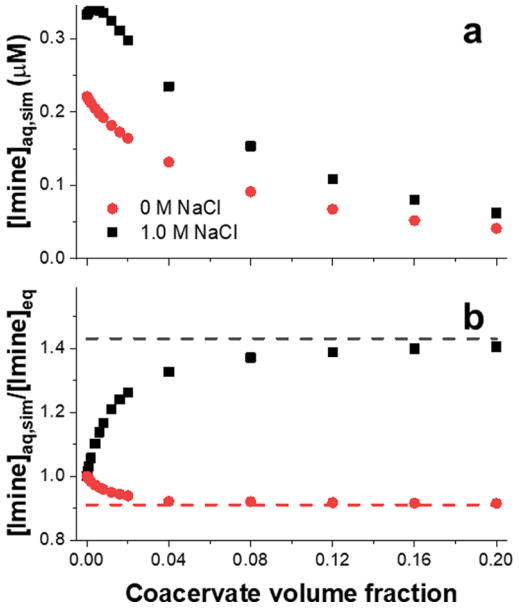

Figure 7. Aqueous composition from imine synthesis in a PAA-PEG coacervate drop (10 μm radius) as a function of coacervate volume fraction. (a) Aqueous imine concentration decreases with increasing coacervate volume fraction at both 0 and 1.0 M NaCl. (b) Relative shift in aqueous imine reaction equilibrium constant at different PAA-PEG volume fractions in 0 and 1.0 M NaCl. The dashed line represents the asymptotic shift in aqueous reaction equilibrium where coacervate reaction and partition equilibria predict the same concentration of imine **3**.

In order to understand how reversible reactions in coacervates can affect bulk solution reactivity, $[\text{imine}]_{\text{aq,sim}}$ was compared to the imine **3** concentration predicted by the aqueous concentration of reactants and $K_{rxn,aq}$ ($[\text{imine}]_{\text{aq,eq}}$). Here, the ratio of $[\text{imine}]_{\text{aq,sim}}$ to $[\text{imine}]_{\text{aq,eq}}$ gives the

https://doi.org/10.1021/acs.langmuir.1c02231
Langmuir 2021, 37, 14323−14335

fractional change in the apparent equilibrium constant due to the reaction in coacervates. If the ratio of $[\text{imine}]_{aq,sim}$ to $[\text{imine}]_{aq,eq}$ is greater than unity, then the aqueous imine **3** concentration is larger than that predicted by $K_{rxn,aq}$ and reactions in coacervates boosted solution reactivity. Conversely, if the ratio is less than unity, then the aqueous imine **3** concentration is smaller than that predicted by $K_{rxn,aq}$ and coacervates lower solution reactivity. Interestingly, our results show that reaction and partition equilibria predict nearly the same imine **3** concentration in the coacervate droplet in the case of 0 M NaCl solution, such that the ratio of $[\text{imine}]_{aq,sim}$ to $[\text{imine}]_{aq,eq}$ is close to 1 at all f_{coac}'s (Figure 7b). These observations suggest that enhanced reactivity and large concentrations of imine **3** in coacervate droplets do not necessarily boost reactivity in aqueous solution. On the other hand, when reaction equilibrium predicts a larger imine **3** concentration than that predicted by partitioning equilibrium such as in the case of 1.0 M NaCl solutions, then there is a net flow of imine **3** out of the coacervate droplet to establish partitioning equilibrium (Figure 7b). In this case, the ratio of $[\text{imine}]_{aq,sim}$ to $[\text{imine}]_{aq,eq}$ is greater than unity and increases with larger values of f_{coac} (Figure 7b). This ratio asymptotically approaches the ratio of $[\text{imine}]_{eq,rxn}$ to $[\text{imine}]_{eq,part}$. In this way, there is a net flow of imine **3** from PAA-PEG coacervate droplets at 1.0 M NaCl until the aqueous concentration increases, such that partitioning and reaction equilibria predict the same concentration of products. Although this asymptotic relationship is expected to be universal for reversible reactions in coacervate droplets, the system behavior is dependent on the characteristics of the reaction and coacervate. For example, increasing droplet size inhibits the ability for coacervate droplets to shift reaction equilibrium in aqueous solution due to their smaller surface-to-volume ratios, which slows diffusional flux between the two phases (Figure S11). Thus, the ability for coacervate droplets to change bulk solution reactivity strongly depends on both molecular transport and how reaction energetics shift within the coacervate.

The reaction−diffusion model was further used to understand how changing *Da* affects the internal distribution of reaction products within a coacervate droplet. Although the reaction rate inside the coacervate droplets is constant, *Da* is varied by changing r_{coac}. At small r_{coac}, diffusional mixing is fast and *Da* is small. Conversely, at large r_{coac}, diffusional mixing is slow and *Da* is large. Similar to the results with changing volume fraction, two scenarios are described: imine synthesis in PAA-PEG coacervates in 0 and 1.0 M NaCl. Simulations were performed at different r_{coac} values with a small volume fraction of $f_{coac} = 1 \times 10^{-4}$ using the kinetic parameters described in Table S2. Figure 8a shows the equilibrium imine **3** concentration in coacervate droplets of different sizes at 0 M NaCl (i.e., conditions in which partition and reaction equilibria give roughly the same concentration of products). In this scenario, the concentration of imine within the coacervate droplet remains roughly constant for all r_{coac} values, and slow transport to the interface does not significantly influence imine **3** concentration. Conversely, in 1 M NaCl (when $[\text{imine}]_{eq,rxn}$ is larger than $[\text{imine}]_{eq,part}$), steep chemical gradients form within the coacervate droplet as r_{coac} and hence *Da* both increase (Figure 8b). At small r_{coac}, the concentration of imine **3** at all points within the droplet is given by $[\text{imine}]_{eq,part}$. However, as the r_{coac} increases and diffusional mixing slows, the concentration of the reaction product at the center of the droplet approaches $[\text{imine}]_{eq,rxn}$. At large r_{coac} (and hence large *Da*), the concentration of imine **3** throughout most of the droplet exists at $[\text{imine}]_{eq,rxn}$, and the concentration only approaches $[\text{imine}]_{eq,part}$ close to the droplet interface. Thus, a stable imine **3** chemical gradient and spatial heterogeneity can form within the coacervate droplets when *Da* is greater than 1. Although not explicitly included in the model, coacervate droplet coalescence leads to larger droplets (and hence larger *Da*) and would promote the formation of chemical spatial heterogeneity. Ultimately, chemistry and the distribution of small molecule reaction products within a coacervate droplet are only understood with careful characterization of both reaction kinetics and transport in both phases of a coacervate system.

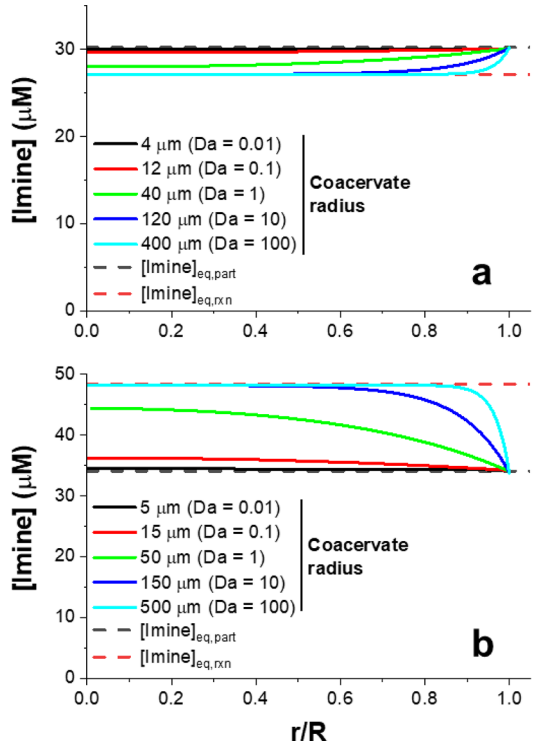

Figure 8. Reaction−diffusion model simulations of radial distribution of imine **3** concentration for differently sized coacervate droplets at low volume fraction (1×10^{-4}) in (a) 0 M and (b) 1.0 M NaCl. The dashed black line shows the concentration of imine **3** predicted by partitioning equilibrium. The dashed red line shows the concentration of imine **3** predicted by reaction equilibrium. Steep chemical gradients form within the coacervate droplet when $Da > 1$ and $[\text{imine}]_{eq,part} \neq [\text{imine}]_{eq,rxn}$.

CONCLUSIONS

In this work, we systematically describe how reaction kinetics and energetics of a reversible bimolecular chemical reaction (imine synthesis) change inside coacervate droplets compared to bulk solution. The concentration of imine **3** was found to be approximately 100−140 times larger in coacervate droplets compared to bulk solution under all solution conditions measured here. The large concentrations of imine **3** observed in coacervate droplets are not achievable in bulk solution due to the low aqueous solubility of the reactants (amine **1** and aldehyde **2**) and the small reaction equilibrium constant $K_{rxn,aq}$. The enhanced imine **3** concentration within coacervate droplets arose from both preferential partitioning of reactants and products into the coacervate phase and a slight shift in the

https://doi.org/10.1021/acs.langmuir.1c02231
Langmuir 2021, 37, 14323−14335

reaction equilibrium constant within coacervates to favor product formation. Depending on the solution condition, $K_{rxn,coac}$ was measured to be roughly 2−3 times larger than $K_{rxn,aq}$. The shift in the equilibrium constant was understood to arise from acid-catalyzed promotion of imine **3** driven by the high concentration of PAA in the coacervate droplet.[40] Thus, through increased reactant concentrations and shifted reaction energetics, coacervate droplets can act as micro-reactors capable of abiotically promoting reversible bimolecular reactions to form larger, higher energy molecules (i.e., increase molecular complexity).

The synthesis of fluorescent imine demonstrates how stable concentration gradients form from reversible reactions inside coacervate droplets, and further, how coacervate droplets can change the chemical composition of the surrounding medium. Because coacervate droplets are membraneless compartments, molecules diffuse freely across the liquid−liquid interface and within the droplet. However, coacervate droplets can also be highly viscous, leading to slow diffusion. The competition between partitioning and reaction equilibrium leads to chemical gradients within a droplet, potentially making product quantification within a coacervate droplet difficult to understand. In the limit of $Da \gg 1$, spatial chemical gradients form inside coacervate droplets, which leads to a difference in the product concentration predicted by reaction and partitioning equilibria. In this case, a net flow of product between the two phases will attempt to equalize reaction and partitioning equilibria. Depending on the concentration of the coacervate droplets in solution, this can result in an apparent shift in reaction equilibrium in the surrounding aqueous solution. Ultimately, measurements of both reaction and transport are necessary to understand reaction kinetics and the spatial distribution of reaction products within coacervate droplets.

Shifts in reaction equilibria and larger concentrations of products from the imine synthesis reaction in coacervate droplets demonstrate how compartmentalization in coacervate droplets might provide a mechanism to drive energetically and kinetically unfavorable reactions in aqueous solution. Although the imine synthesis reaction leads to a modest increase in molecular complexity, the ability for coacervates to sequester a wide variety of small molecules could promote multiple different reaction pathways to drastically increase chemical complexity. Thus, these results may suggest a mechanism by which coacervate droplets could promote abiotic synthetic chemistry to produce autocatalytic molecular species relevant to the origin of life.[55] In addition, given that substrate interactions with macromolecules in a molecularly crowded environment can affect enzyme kinetics,[36] the results here demonstrate how coacervate droplets could promote substrate channeling in enzymatic reaction pathways by slightly stabilizing labile intermediates.[39] Our results suggest that, beyond the biomolecular processes that are typically studied,[9] compartmentalization within coacervates can potentially influence or accelerate a wide variety of small molecule reactions.

■ ASSOCIATED CONTENT

Supporting Information

The Supporting Information is available free of charge at https://pubs.acs.org/doi/10.1021/acs.langmuir.1c02231.

Synthetic details and the ^{1}H NMR spectra of all molecules; definitions of variables; additional details on reaction rate quantification; detailed description of the reaction−diffusion model, parameters used in the model, and additional model results; comparison of imine **3** and dye **4** relative quantum yields; dye **4** molar absorptivity plot; PEG-PAA coacervate turbidity analysis; the UV−vis spectra of reactants; plots of K_{rxn} under different solution conditions; the UV−vis spectra of imine **3** in coacervates; diffusion coefficient measurements; calculated K_{OW} of reactants and products (PDF)

■ AUTHOR INFORMATION

Corresponding Author

Charles M. Schroeder − *Beckman Institute for Advanced Science and Technology, Department of Chemical and Biomolecular Engineering, and Department of Materials Science and Engineering, University of Illinois at Urbana-Champaign, Urbana, Illinois 61801, United States;* orcid.org/0000-0001-6023-2274; Email: cms@illinois.edu

Authors

Michael I. Jacobs − *Beckman Institute for Advanced Science and Technology, University of Illinois at Urbana-Champaign, Urbana, Illinois 61801, United States*

Edward R. Jira − *Beckman Institute for Advanced Science and Technology and Department of Chemical and Biomolecular Engineering, University of Illinois at Urbana-Champaign, Urbana, Illinois 61801, United States*

Complete contact information is available at: https://pubs.acs.org/10.1021/acs.langmuir.1c02231

Notes

The authors declare no competing financial interest.

■ ACKNOWLEDGMENTS

This work was supported by the National Science Foundation under grant no. CBET-2030537 for C.M.S. and a Beckman Institute Postdoctoral Fellowship to M.I.J.

■ REFERENCES

(1) Banani, S. F.; Lee, H. O.; Hyman, A. A.; Rosen, M. K. Biomolecular Condensates: Organizers of Cellular Biochemistry. *Nat. Rev. Mol. Cell Biol.* **2017**, *18*, 285−298.

(2) Li, P.; Banjade, S.; Cheng, H. C.; Kim, S.; Chen, B.; Guo, L.; Llaguno, M.; Hollingsworth, J. V.; King, D. S.; Banani, S. F.; Russo, P. S.; Jiang, Q. X.; Nixon, B. T.; Rosen, M. K. Phase Transitions in the Assembly of Multivalent Signalling Proteins. *Nature* **2012**, *483*, 336−340.

(3) Su, X.; Ditlev, J. A.; Hui, E.; Xing, W.; Banjade, S.; Okrut, J.; King, D. S.; Taunton, J.; Rosen, M. K.; Vale, R. D. Phase Separation of Signaling Molecules Promotes T Cell Receptor Signal Transduction. *Science* **2016**, *352*, 595−599.

(4) Berry, J.; Weber, S. C.; Vaidya, N.; Haataja, M.; Brangwynne, C. P.; Weitz, D. A. RNA Transcription Modulates Phase Transition-Driven Nuclear Body Assembly. *Proc. Natl. Acad. Sci. U. S. A.* **2015**, *112*, E5237−E5245.

(5) Boija, A.; Klein, I. A.; Sabari, B. R.; Dall'Agnese, A.; Coffey, E. L.; Zamudio, A. V.; Li, C. H.; Shrinivas, K.; Manteiga, J. C.; Hannett, N. M.; Abraham, B. J.; Afeyan, L. K.; Guo, Y. E.; Rimel, J. K.; Fant, C. B.; Schuijers, J.; Lee, T. I.; Taatjes, D. J.; Young, R. A. Transcription Factors Activate Genes through the Phase-Separation Capacity of Their Activation Domains. *Cell* **2018**, *175*, 1842−1855.e16.

(6) Alberti, S. The Wisdom of Crowds: Regulating Cell Function through Condensed States of Living Matter. *J. Cell Sci.* **2017**, *130*, 2789−2796.
(7) Mann, S. Systems of Creation: The Emergence of Life from Nonliving Matter. *Acc. Chem. Res.* **2012**, *45*, 2131−2141.
(8) Keating, C. D. Aqueous Phase Separation as a Possible Route to Compartmentalization of Biological Molecules. *Acc. Chem. Res.* **2012**, *45*, 2114−2124.
(9) Nakashima, K. K.; Vibhute, M. A.; Spruijt, E. Biomolecular Chemistry in Liquid Phase Separated Compartments. *Front. Mol. Biosci.* **2019**, *6*, 1−9.
(10) Yewdall, N. A.; André, A. A. M.; Lu, T.; Spruijt, E. Coacervates as Models of Membraneless Organelles. *Curr. Opin. Colloid Interface Sci.* **2021**, *52*, 101416.
(11) Aumiller, W. M., Jr.; Keating, C. D. Experimental Models for Dynamic Compartmentalization of Biomolecules in Liquid Organelles: Reversible Formation and Partitioning in Aqueous Biphasic Systems. *Adv. Colloid Interface Sci.* **2017**, *239*, 75−87.
(12) Sing, C. E.; Perry, S. L. Recent Progress in the Science of Complex Coacervation. *Soft Matter* **2020**, *16*, 2885−2914.
(13) O'Flynn, B. G.; Mittag, T. The Role of Liquid−Liquid Phase Separation in Regulating Enzyme Activity. *Curr. Opin. Cell Biol.* **2021**, *69*, 70−79.
(14) Stroberg, W.; Schnell, S. Do Cellular Condensates Accelerate Biochemical Reactions? Lessons from Microdroplet Chemistry. *Biophys. J.* **2018**, *115*, 3−8.
(15) Koga, S.; Williams, D. S.; Perriman, A. W.; Mann, S. Peptide-Nucleotide Microdroplets as a Step towards a Membrane-Free Protocell Model. *Nat. Chem.* **2011**, *3*, 720−724.
(16) Strulson, C. A.; Molden, R. C.; Keating, C. D.; Bevilacqua, P. C. RNA Catalysis through Compartmentalization. *Nat. Chem.* **2012**, *4*, 941.
(17) Crosby, J.; Treadwell, T.; Hammerton, M.; Vasilakis, K.; Crump, M. P.; Williams, D. S.; Mann, S. Stabilization and Enhanced Reactivity of Actinorhodin Polyketide Synthase Minimal Complex in Polymer−Nucleotide Coacervate Droplets. *Chem. Commun.* **2012**, *48*, 11832−11834.
(18) Poudyal, R. R.; Guth-metzler, R. M.; Veenis, A. J.; Frankel, E. A.; Keating, C. D.; Bevilacqua, P. C. Template-Directed RNA Polymerization and Enhanced Ribozyme Catalysis inside Membraneless Compartments Formed by Coacervates. *Nat. Commun.* **2019**, *10*, 490.
(19) Küffner, A. M.; Prodan, M.; Zuccarini, R.; Capasso Palmiero, U.; Faltova, L.; Arosio, P. Acceleration of an Enzymatic Reaction in Liquid Phase Separated Compartments Based on Intrinsically Disordered Protein Domains. *ChemSystemsChem* **2020**, *2*, 1−7.
(20) Altenburg, W. J.; Yewdall, N. A.; Vervoort, D. F. M.; van Stevendaal, M. H. M. E.; Mason, A. F.; van Hest, J. C. M. Programmed Spatial Organization of Biomacromolecules into Discrete, Coacervate-Based Protocells. *Nat. Commun.* **2020**, *11*, 6282.
(21) Drobot, B.; Iglesias-Artola, J. M.; Le Vay, K.; Mayr, V.; Kar, M.; Kreysing, M.; Mutschler, H.; Tang, T. Y. D. Compartmentalised RNA Catalysis in Membrane-Free Coacervate Protocells. *Nat. Commun.* **2018**, *9*, 3643.
(22) Poudyal, R. R.; Keating, C. D.; Bevilacqua, P. C. Polyanion-Assisted Ribozyme Catalysis Inside Complex Coacervates. *ACS Chem. Biol.* **2019**, *14*, 1243−1248.
(23) Sokolova, E.; Spruijt, E.; Hansen, M. M. K.; Dubuc, E.; Groen, J.; Chokkalingam, V.; Piruska, A.; Heus, H. A.; Huck, W. T. S. Enhanced Transcription Rates in Membrane-Free Protocells Formed by Coacervation of Cell Lysate. *Proc. Natl. Acad. Sci. U. S. A.* **2013**, *110*, 11692−11697.
(24) Peeples, W.; Rosen, M. K. Mechanistic Dissection of Increased Enzymatic Rate in a Phase-Separated Compartment. *Nat. Chem. Biol.* **2021**, *17*, 693−702.
(25) Aumiller, W. M., Jr.; Davis, B. W.; Hashemian, N.; Maranas, C.; Armaou, A.; Keating, C. D. Coupled Enzyme Reactions Performed in Heterogeneous Reaction Media: Experiments and Modeling for Glucose Oxidase and Horseradish Peroxidase in a PEG/Citrate Aqueous Two-Phase System. *J. Phys. Chem. B* **2014**, *118*, 2506−2517.
(26) Davis, B. W.; Aumiller, W. M., Jr.; Hashemian, N.; An, S.; Armaou, A.; Keating, C. D. Colocalization and Sequential Enzyme Activity in Aqueous Biphasic Systems: Experiments and Modeling. *Biophys. J.* **2015**, *109*, 2182−2194.
(27) Chen, Y.; Yuan, M.; Zhang, Y.; Liu, S.; Yang, X.; Wang, K.; Liu, J. Construction of Coacervate-in-Coacervate Multi-Compartment Protocells for Spatial Organization of Enzymatic Reactions. *Chem. Sci.* **2020**, *11*, 8617−8625.
(28) Lv, K.; Perriman, A. W.; Mann, S. Photocatalytic Multiphase Micro-Droplet Reactors Based on Complex Coacervation. *Chem. Commun.* **2015**, *51*, 8600−8602.
(29) Pir Cakmak, F.; Keating, C. D. Combining Catalytic Microparticles with Droplets Formed by Phase Coexistence: Adsorption and Activity of Natural Clays at the Aqueous/Aqueous Interface. *Sci. Rep.* **2017**, *7*, 3215.
(30) Tang, T. Y. D.; Antognozzi, M.; Vicary, J. A.; Perriman, A. W.; Mann, S. Small-Molecule Uptake in Membrane-Free Peptide/Nucleotide Protocells. *Soft Matter* **2013**, *9*, 7647−7656.
(31) Zhao, M.; Zacharia, N. S. Sequestration of Methylene Blue into Polyelectrolyte Complex Coacervates. *Macromol. Rapid Commun.* **2016**, *37*, 1249−1255.
(32) Zhao, M.; Eghtesadi, S. A.; Dawadi, M. B.; Wang, C.; Huang, S.; Seymore, A. E.; Vogt, B. D.; Modarelli, D. A.; Liu, T.; Zacharia, N. S. Partitioning of Small Molecules in Hydrogen-Bonding Complex Coacervates of Poly(Acrylic Acid) and Poly(Ethylene Glycol) or Pluronic Block Copolymer. *Macromolecules* **2017**, *50*, 3818−3830.
(33) Huang, S.; Zhao, M.; Dawadi, M. B.; Cai, Y.; Lapitsky, Y.; Modarelli, D. A.; Zacharia, N. S. Effect of Small Molecules on the Phase Behavior and Coacervation of Aqueous Solutions of Poly(Diallyldimethylammonium Chloride) and Poly(Sodium 4-Styrene Sulfonate). *J. Colloid Interface Sci.* **2018**, *518*, 216−224.
(34) Lu, T.; Spruijt, E. Multiphase Complex Coacervate Droplets. *J. Am. Chem. Soc.* **2020**, *142*, 2905−2914.
(35) Mountain, G. A.; Keating, C. D. Formation of Multiphase Complex Coacervates and Partitioning of Biomolecules within Them. *Biomacromolecules* **2020**, *21*, 630−640.
(36) Aumiller, W. M., Jr.; Davis, B. W.; Hatzakis, E.; Keating, C. D. Interactions of Macromolecular Crowding Agents and Cosolutes with Small-Molecule Substrates: Effect on Horseradish Peroxidase Activity with Two Different Substrates. *J. Phys. Chem. B* **2014**, *118*, 10624−10632.
(37) Li, L.; Srivastava, S.; Andreev, M.; Marciel, A. B.; De Pablo, J. J.; Tirrell, M. V. Phase Behavior and Salt Partitioning in Polyelectrolyte Complex Coacervates. *Macromolecules* **2018**, *51*, 2988−2995.
(38) Nott, T. J.; Petsalaki, E.; Farber, P.; Jervis, D.; Fussner, E.; Plochowietz, A.; Craggs, T. D.; Bazett-Jones, D. P.; Pawson, T.; Forman-Kay, J. D.; Baldwin, A. J. Phase Transition of a Disordered Nuage Protein Generates Environmentally Responsive Membraneless Organelles. *Mol. Cell* **2015**, *57*, 936−947.
(39) Castellana, M.; Wilson, M. Z.; Xu, Y.; Joshi, P.; Cristea, I. M.; Rabinowitz, J. D.; Gitai, Z.; Wingreen, N. S. Enzyme Clustering Accelerates Processing of Intermediates through Metabolic Channeling. *Nat. Biotechnol.* **2014**, *32*, 1011−1018.
(40) Chen, C.; Tan, J.; Hsieh, M.-C.; Pan, T.; Goodwin, J. T.; Mehta, A. K.; Grover, M. A.; Lynn, D. G. Design of Multi-Phase Dynamic Chemical Networks. *Nat. Chem.* **2017**, *9*, 799−804.
(41) Khutoryanskiy, V. V.; Dubolazov, A. V.; Nurkeeva, Z. S.; Mun, G. A. PH Effects in the Complex Formation and Blending of Poly(Acrylic Acid) with Poly(Ethylene Oxide). *Langmuir* **2004**, *20*, 3785−3790.
(42) Meguellati, K.; Spichty, M.; Ladame, S. Reversible Synthesis and Characterization of Dynamic Imino Analogues of Trimethine and Pentamethine Cyanine Dyes. *Org. Lett.* **2009**, *11*, 1123−1126.
(43) Meguellati, K.; Fallah-araghi, A.; Baret, J.; Harrak, E. Enhanced Imine Synthesis in Water: From Surfactant- Mediated Catalysis to Host−Guest Mechanisms. 2013, 11332−11334, DOI: 10.1039/c3cc46461j.

(44) Li, D.; Tian, X.; Wang, A.; Guan, L.; Zheng, J.; Li, F.; Li, S.; Zhou, H.; Wu, J.; Tian, Y. Nucleic Acid-Selective Light-up Fluorescent Biosensors for Ratiometric Two-Photon Imaging of the Viscosity of Live Cells and Tissues. *Chem. Sci.* **2016**, *7*, 2257−2263.
(45) Jia, T. Z.; Hentrich, C.; Szostak, J. W. Rapid RNA Exchange in Aqueous Two-Phase System and Coacervate Droplets. *Orig. Life Evol. Biosph.* **2014**, *44*, 1−12.
(46) Axelrod, D.; Koppel, D. E.; Schlessinger, J.; Elson, E.; Webb, W. W. Mobility Measurement by Analysis of Fluorescence Photobleaching Recovery Kinetics. *Biophys. J.* **1976**, *16*, 1055−1069.
(47) Sprague, B. L.; Pego, R. L.; Stavreva, D. A.; McNally, J. G. Analysis of Binding Reactions by Fluorescence Recovery after Photobleaching. *Biophys. J.* **2004**, *86*, 3473−3495.
(48) Peters, M.; Eckstein, M. F.; Hartjen, G.; Spiess, A. C.; Leitner, W.; Greiner, L. Exploring Conversion of Biphasic Catalytic Reactions: Analytical Solution and Parameter Study. *Ind. Eng. Chem. Res.* **2007**, *46*, 7073−7078.
(49) Fallah-Araghi, A.; Meguellati, K.; Baret, J.-C.; Harrak, A. E.; Mangeat, T.; Karplus, M.; Ladame, S.; Marques, C. M.; Griffiths, A. D. Enhanced Chemical Synthesis at Soft Interfaces: A Universal Reaction-Adsorption Mechanism in Microcompartments. *Phys. Rev. Lett.* **2014**, *112*, No. 028301.
(50) Wilson, K. R.; Prophet, A. M.; Rovelli, G.; Willis, M. D.; Rapf, R. J.; Jacobs, M. I. A Kinetic Description of How Interfaces Accelerate Reactions in Micro-Compartments. *Chem. Sci.* **2020**, *11*, 8533−8545.
(51) Das, K. K.; Somasundaran, P. Ultra-Low Dosage Flocculation of Alumina Using Polyacrylic Acid. *Colloids Surf. A Physicochem. Eng. Asp.* **2001**, *182*, 25−33.
(52) Tetko, I. V.; Gasteiger, J.; Todeschini, R.; Mauri, A.; Livingstone, D.; Ertl, P.; Palyulin, V. A.; Radchenko, E. V.; Zefirov, N. S.; Makarenko, A. S.; Tanchuk, V. Y.; Prokopenko, V. V. Virtual Computational Chemistry Laboratory - Design and Description. *J. Comput.-Aided Mol. Des.* **2005**, *19*, 453−463.
(53) Fares, H. M.; Marras, A. E.; Ting, J. M.; Tirrell, M. V.; Keating, C. D. Impact of Wet-Dry Cycling on the Phase Behavior and Compartmentalization Properties of Complex Coacervates. *Nat. Commun.* **2020**, *11*, 5423.
(54) Chloë Bulinski, J.; Odde, D. J.; Howell, B. J.; Salmon, T. D.; Waterman-Storer, C. M. Rapid Dynamics of the Microtubule Binding of Ensconsin in Vivo. *J. Cell Sci.* **2001**, *114*, 3885−3897.
(55) Chen, I. A.; Nowak, M. A. From Prelife to Life: How Chemical Kinetics Become Evolutionary Dynamics. *Acc. Chem. Res.* **2012**, *45*, 2088−2096.

https://doi.org/10.1021/acs.langmuir.1c02231
Langmuir 2021, 37, 14323−14335